Paramagnetic Solid-State NMR to Localize the Metal-Ion Cofactor in an Oligomeric DnaB Helicase

Johannes Zehnder,[a] Riccardo Cadalbert,[a] Laurent Terradot,[b] Matthias Ernst,[a] Anja Böckmann,[b] Peter Güntert,*[a, c, d] Beat H. Meier,*[a] and Thomas Wiegand*[a]

Abstract: Paramagnetic metal ions can be inserted into ATP-fueled motor proteins by exchanging the diamagnetic Mg^{2+} cofactor with Mn^{2+} or Co^{2+}. Then, paramagnetic relaxation enhancement (PRE) or pseudo-contact shifts (PCSs) can be measured to report on the localization of the metal ion within the protein. We determine the metal position in the oligomeric bacterial DnaB helicase from *Helicobacter pylori* complexed with the transition-state ATP-analogue ADP:AlF$_4^-$ and single-stranded DNA using solid-state NMR and a structure-calculation protocol employing CYANA. We discuss and compare the use of Mn^{2+} and Co^{2+} in localizing the ATP cofactor in large oligomeric protein assemblies. ^{31}P PCSs induced in the Co^{2+}-containing sample are then used to localize the DNA phosphate groups on the Co^{2+} PCS tensor surface enabling structural insights into DNA binding to the DnaB helicase.

Introduction

NMR spectroscopy in the solution state has been used extensively for structural and dynamic studies of nucleotide-bound proteins. Often chemical-shift perturbations (CSPs) serve as a convenient tool to identify protein-nucleotide binding sites.[1] Because CSPs are sensitive to conformational changes, they can also be caused by allosteric effects which makes the determination of the position of the bound nucleotide in the protein difficult.[2] Paramagnetic centers instead lead to paramagnetic relaxation enhancement (PRE) and pseudo-contact shifts (PCS). For both effects, observed changes upon metal exchange depend directly on the distance between the paramagnetic center and the residue of interest of the protein.[3]

The DnaB helicase from *Helicobacter pylori* is a double-hexameric motor protein which couples ATP hydrolysis to mechanical motion.[4,5] Since ATP-binding is accompanied by the binding of Mg^{2+},[6] substitution of Mg^{2+} by paramagnetic ions, such as Mn^{2+} or Co^{2+}, allows us to introduce paramagnetic probes into the protein assembly. This approach is commonly applied in NMR as well as EPR and paramagnetic effects are often used in structure calculation protocols.[7–16] The oligomeric character of DnaB and thus its inherent size, limit however the use of solution-state NMR due to the broadening of the lines induced by fast T_2 relaxation for slowly tumbling large proteins (life-time broadening effects).[17,18] Solid-state NMR is not affected by this size limitation and offers also significant advantages compared to X-ray crystallography in that it is well-suited for the investigation of difficult-(or even impossible)-to-crystallize biomolecular assemblies.[19] For solid-state NMR sample preparation, the protein complexes can simply be sedimented into the NMR rotor.[20–23]

In NMR spectra paramagnetic NMR effects encode information on electron-nucleus distances on the length scale of ~20 Å,[3] for some lanthanide tags even up to 40 Å.[24] Paramagnetic metal ions with an anisotropic magnetic susceptibility tensor induce, via the electron-nucleus dipolar coupling (spin-dipolar interaction), a contribution to the isotropic chemical shift.[25] This isotropic contribution is called pseudo-contact shift and is given within the metal-centered point-dipole approximation by (same for solution and solid state):

$$\delta^{PCS} = \frac{1}{12\pi r^3}\left[\Delta\chi_{ax}(3cos^2\theta - 1) + \frac{3}{2}\Delta\chi_{rh}sin^2\theta\ cos2\varphi\right] \tag{1}$$

where r is the electron-nucleus distance, θ and φ are the polar and azimuthal angles which describe the orientation of the electron-nucleus vector in the principle axis frame of the $\Delta\chi$-tensor,[26–28] and $\Delta\chi_{ax}$ and $\Delta\chi_{rh}$ are the axial and rhombic

[a] J. Zehnder, R. Cadalbert, Prof. M. Ernst, Prof. P. Güntert, Prof. B. H. Meier, Dr. T. Wiegand
Laboratorium für Physikalische Chemie
ETH Zürich, Vladimir-Prelog-Weg 2, 8093 Zürich (Switzerland)
E-mail: peter.guentert@phys.chem.ethz.ch
beme@ethz.ch
thomas.wiegand@phys.chem.ethz.ch

[b] Dr. L. Terradot, Dr. A. Böckmann
IBCP BMSSI, 7 Passage du Vercors, 69007 Lyon (France)

[c] Prof. P. Güntert
Institute of Biophysical Chemistry, Center for Biomolecular Magnetic Resonance
Goethe University Frankfurt am Main, 60438 Frankfurt am Main (Germany)

[d] Prof. P. Güntert
Department of Chemistry, Tokyo Metropolitan University
Hachioji, Tokyo 1920397 (Japan)

Supporting information for this article is available on the WWW under https://doi.org/10.1002/chem.202100462

Chemistry–A European Journal

Full Paper
doi.org/10.1002/chem.202100462

Chemistry Europe
European Chemical
Societies Publishing

anisotropy parameters of the $\Delta\chi$-tensor which are given in terms of the Cartesian tensor components by

$$\Delta\chi_{ax} = \chi_{zz} - \frac{\chi_{xx} + \chi_{yy}}{2}, \; \Delta\chi_{rh} = \chi_{xx} - \chi_{yy} \tag{2}$$

The PCSs typically range in between a few tens of ppm's up to several ppm. Furthermore, the orientation dependence induces positive or negative PCSs. There is an additional anisotropic contribution of the electron-nucleus dipolar coupling which, in contrast to the PCSs, is averaged by MAS, but still might be significant for residues in close vicinity to the metal center at typical MAS frequencies used (*vide infra*).

Stochastic modulation of the hyperfine coupling between the unpaired electron(s) and the nuclei provides a relaxation pathway, the paramagnetic nuclear relaxation enhancements (PREs), that leads to enhanced longitudinal nuclear T_1 relaxation as well as rotating-frame $T_{1\rho}$ relaxation and transverse relaxation T_2, when compared to the diamagnetic equivalent. In the context of the Solomon-Bloembergen relaxation theory[29,30] the enhancements of dipolar longitudinal and transverse relaxation rates $\Gamma = T^{-1}$ can be approximated by

$$\Gamma_1 = \frac{2}{15}\left(\frac{\mu_0}{4\pi}\right)^2 \frac{\gamma_n^2 g_e^2 \beta^2 S(S+1)}{r^6} \left(\frac{3T_{1e}}{1+\omega_n^2 T_{1e}^2} + \frac{7T_{2e}}{1+\omega_e^2 T_{2e}^2}\right) \tag{3}$$

$$\Gamma_{1\rho} \approx \Gamma_2 = \frac{1}{15}\left(\frac{\mu_0}{4\pi}\right)^2 \frac{\gamma_n^2 g_e^2 \beta^2 S(S+1)}{r^6} \cdot \left(4T_{1e} + \frac{3T_{1e}}{1+\omega_n^2 T_{1e}^2} + \frac{13T_{2e}}{1+\omega_e^2 T_{2e}^2}\right) \tag{4}$$

assuming that $\omega_e \gg \omega_n$ and that the correlation time is approximated by the longitudinal electron spin relaxation time constant T_{1e} (with $T_{1e} \approx T_{2e}$).[3,31] PREs influence the NMR spectra:[26,28,31,32] while the peak height is influenced by both, Γ_1 and Γ_2, the peak integral is only affected by Γ_1. We herein use the peak height (in the following denoted as peak attenuation) to measure the PREs which scale with r^{-6} where r is the electron-nucleus distance (see Eqs. (3) and (4)). Although this does not allow us to quantify Γ_1 and Γ_2, it still allows using PREs as distance restraints in structure calculations. Residues located on a surface of a sphere with radius r experience the same PRE effect. Amino acids located within the so-called blind sphere around the metal center are broadened beyond detection and remain thus completely absent in the NMR spectra. PRE effects can be observed for both, Mn^{2+} and Co^{2+}, although they are expected to be larger for Mn^{2+} due to the shorter T_{1e} relaxation times of Co^{2+} compared with Mn^{2+}.[9,19,33–35] An example using Co^{2+} as a paramagnetic center at a static magnetic field of 20 T showed that all ^{13}C nuclei with a distance of less than 10 Å to the paramagnetic metal ion are broadened beyond detection.[35] Residues in the vicinity of the Co^{2+} metal center experience additional large anisotropic paramagnetic shifts (resulting from the anisotropic part of the hyperfine interaction[36]) precluding their detection in solid-state NMR spectra at high magnetic fields and slow-to-moderate

MAS frequencies. This mechanism also contributes to the blind sphere radius measured for Co^{2+}.

Results and Discussion

Paramagnetic effects manifested in solid-state NMR spectra

In this work, we focus on DnaB samples complexed with the ATP transition-state analogue $ADP:AlF_4^-$, a metal-ion cofactor, and single-stranded DNA, $(dT)_{20}$, corresponding to the $DnaB:ADP:AlF4^-:DNA$ state previously described.[5] The physiologically relevant complex with the cofactor Mg^{2+} was used as diamagnetic reference state (denoted in the following for the sake of simplicity as $DnaB:Mg^{2+}$), and Mn^{2+} and Co^{2+} for the paramagnetic states (Figure 1a), referred to in the following as $DnaB:Mn^{2+}$ and $DnaB:Co^{2+}$, respectively. Note that DnaB is biologically active with all three metal ions.[32,37] For all three samples the same set of solid-state NMR experiments was recorded, namely 2D ^{13}C-^{13}C 20 ms Dipolar Assisted Rotational Resonance (DARR),[38] 2D NCA[39] and 3D NCACB. Characteristic DARR fingerprints of diamagnetic $DnaB:Mg^{2+}$ and paramagnetic $DnaB:Mn^{2+}$ and $DnaB:Co^{2+}$ complexes are shown in Figure 1 (for the full spectra see Figure S1). The assignment of the diamagnetic sample is transferred from reference.[5] Substitution of the Mg^{2+} cofactor by Mn^{2+} induces significant peak amplitude attenuations in the NMR spectra as a consequence of PREs, as we have recently also shown for DnaB complexed with the pre-hydrolytic ATP mimic AMP-PNP.[32] Three types of resonances can be distinguished in the spectra (Figure 1b and 1c): those unaffected by Mn^{2+} (e.g. T177), those attenuated in signal intensity by Mn^{2+} (e.g. A449 and T450), and those disappearing entirely at the given signal-to-noise level (e.g. S206, A351 and T462). The fact that some peaks disappear completely from the spectra indicates the occupation of the nucleotide-binding sites of all molecules by the metal ion cofactor. In case of Co^{2+}, resonances in the 2D DARR spectra are either unaffected by Co^{2+} (no PCS, e.g. T452), shifted and attenuated by Co^{2+} (e.g. A449 and T450), or disappearing at the given signal-to-noise level (e.g. S206, A382 and T462).

Peak amplitudes in multidimensional solid-state NMR experiments may be influenced by enhancements in longitudinal relaxation-rate constants (Γ_1), longitudinal relaxation-rate constants in the rotating frame ($\Gamma_{1\rho}$) and transverse relaxation-rate constants (Γ_2). It has been shown for GB1 covalently labelled with EDTA-Mn^{2+} that the signal attenuation in MAS experiments is dominated by transverse relaxation during the indirect and direct evolution periods of the NMR experiment.[31] However, a certain attenuation is also due to $\Gamma_{1\rho}$ relaxation during the cross-polarization steps. Peak attenuations in 2D and 3D spectra are different (e.g. due to different numbers of polarization-transfer steps and evolution periods) precluding their direct comparison.

The peak attenuations extracted from 3D NCACB spectra (Figure S2) of diamagnetic $DnaB:Mg^{2+}$ and paramagnetic $DnaB:Mn^{2+}$ are given in Figure 2a. Residues located in the blind sphere of Mn^{2+} are broadened beyond detection in the

Chemistry–A European Journal

Full Paper
doi.org/10.1002/chem.202100462

Chemistry Europe
European Chemical
Societies Publishing

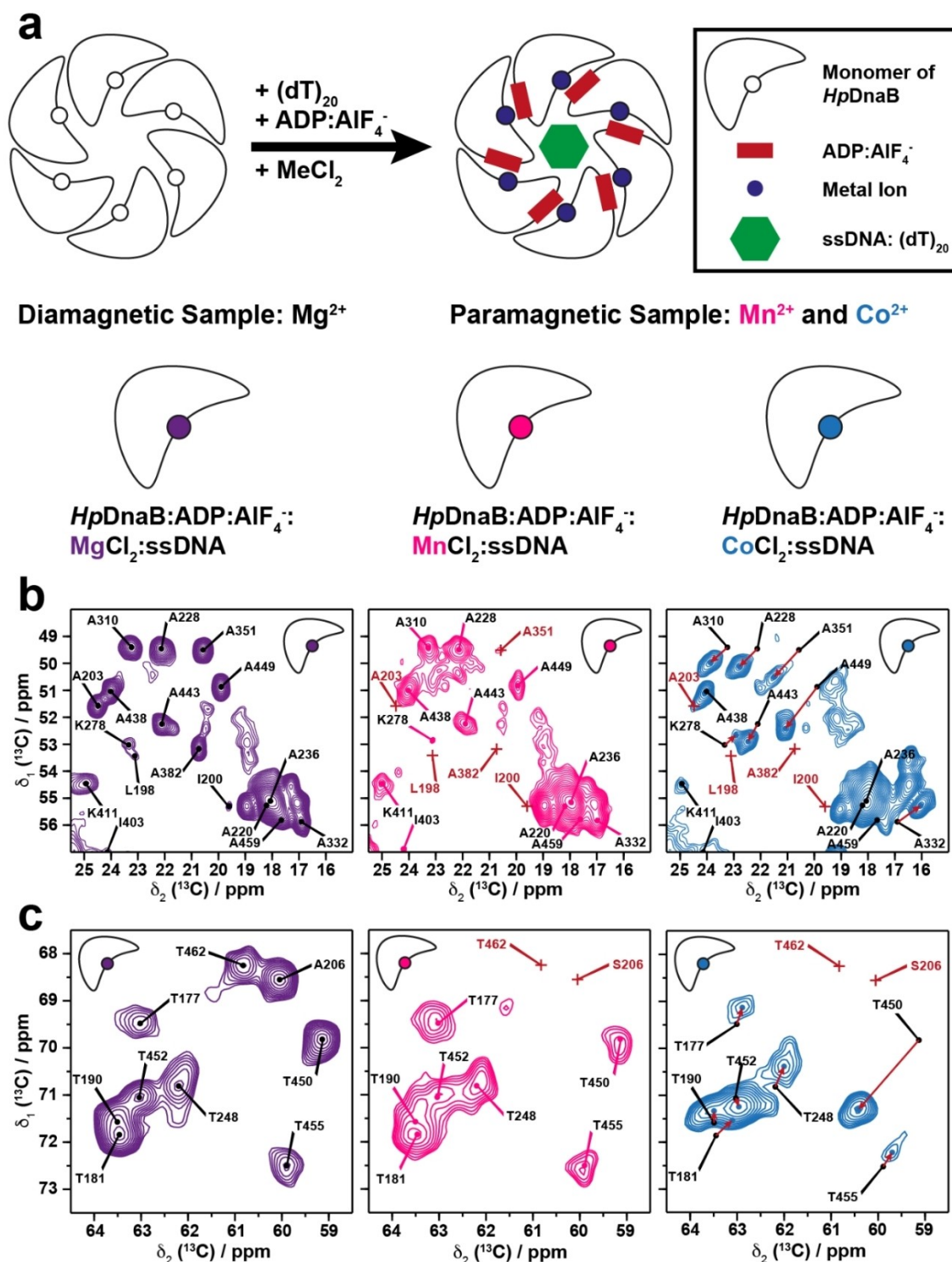**Figure 1.** Substitutions of Mg^{2+} by paramagnetic metal ions and the consequences in the NMR spectra. **a**. Schematic representation of $ADP:AlF_4^-:Me^{2+}$ and DNA binding to HpDnaB. The HpDnaB helicase is shown as a hexamer. **b,c**. 2D $^{13}C–^{13}C$ 20 ms DARR spectra showing **b** the alanine and **c** the threonine region of DnaB:Mg^{2+} (purple), DnaB:Mn^{2+} (pink) and DnaB:Co^{2+} (blue). The peaks which are no longer visible in the paramagnetic spectra are marked with a red cross (e.g. S206, A351 and T462). Changes in line position (PCS) are highlighted by red arrows. Full DARR spectra are shown in Figure S1.

paramagnetic spectrum (highlighted by vertical light red bars). They give rise to long-range distance restraints (upper distance limit of 15 Å, *vide infra*) allowing for the localization of Mn^{2+} in the oligomeric protein assembly. We interpret the relative

intensities of the peaks visible in both spectra only qualitatively (due to the relatively large error bars on the PRE values caused by the limited signal-to-noise ratio in 3D solid-state NMR experiments) and define two classes of PRE restraints, namely
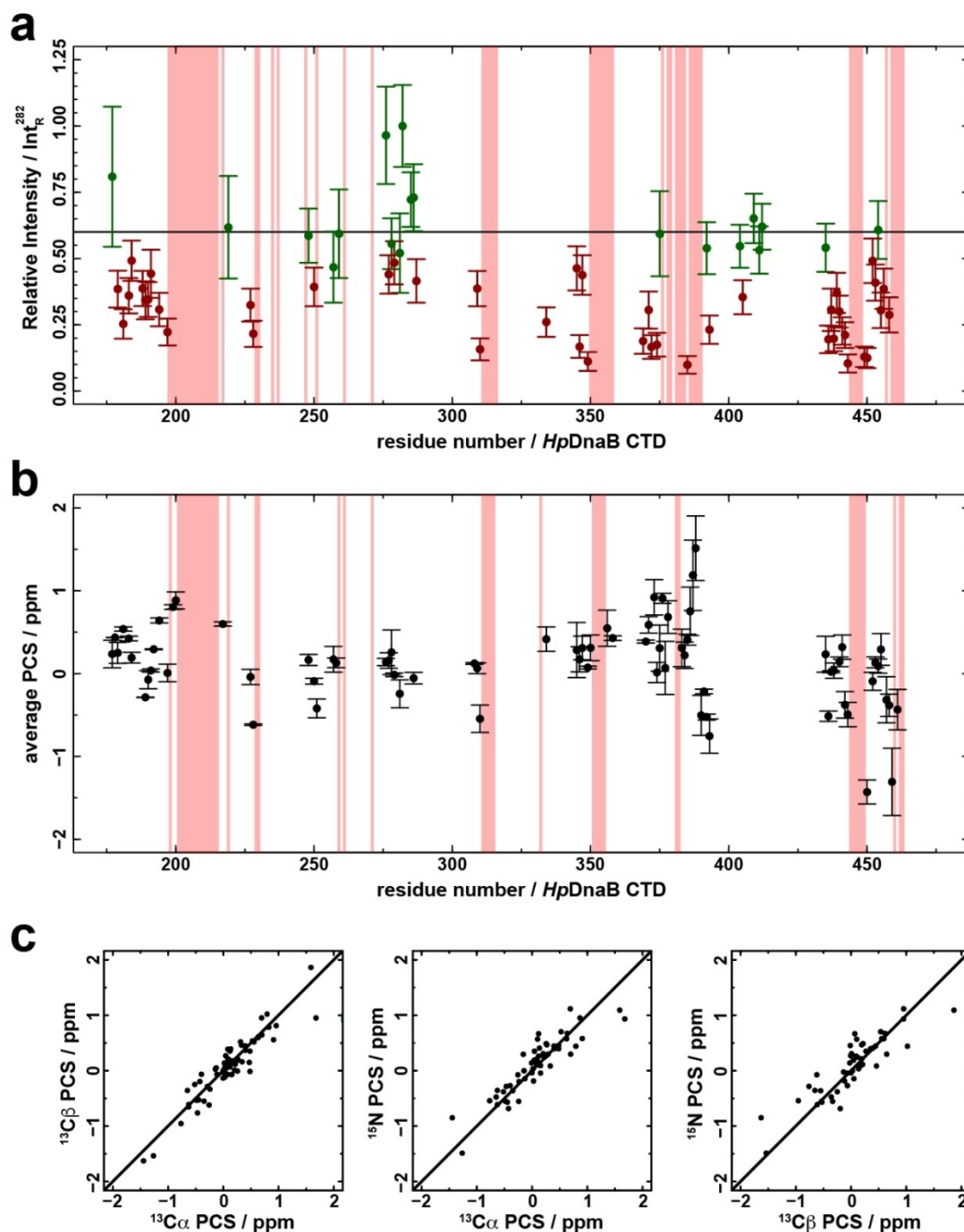
Chemistry–A European Journal

Full Paper
doi.org/10.1002/chem.202100462

**Chemistry
Europe**
European Chemical
Societies Publishing

Figure 2. Overview of site-specific PRE and PCS effects. **a.** PRE effects extracted from 3D NCACB. Residues with peaks vanishing in the paramagnetic spectrum are highlighted by vertical light red bars. Relative intensities I_{para}/I_{dia} are normalized by the relative intensity of F282 which was set to 1.0 (see Methods). The black horizontal line indicates a normalized relative intensity of 0.6 which we consider as the threshold for distinguishing between residues experiencing a significant PRE (< 0.6, data points marked in red) and no significant PRE effect (> 0.6, green).[32] **b.** Average PCS calculated over the assigned ^{15}N, $^{13}C^{\alpha}$ and $^{13}C^{\beta}$ PCS extracted from 2D NCA and 3D NCACB spectra. All residues which are not visible in the paramagnetic spectrum are highlighted by light red bars. **c.** PCS correlations between ^{15}N, $^{13}C^{\alpha}$ and $^{13}C^{\beta}$. Solid lines represent linear regressions (fitted with a slope of 1 and through the origin) with R^2-values of 0.87, 0.81 and 0.77 from the left to the right. Complete PRE and PCS data are available in Tables S1 and S2.

resonances with relative intensities above (residues classified as experiencing no PREs) and below 0.6 (resonance classified as experiencing PREs). The latter peaks lead to a lower distance restraint of 18 Å (*vide infra*).

PCSs were extracted for DnaB:Co^{2+} for the backbone atoms (N, C$^{\alpha}$ and C$^{\beta}$) and were determined from 2D NCA (Figure S3) and 3D NCACB spectra (Figure S2). Average PCSs over the backbone atoms (N, C$^{\alpha}$ and C$^{\beta}$) are given in Figure 2b. The assignment of the DnaB:Co^{2+} sample in the solid state was not

Chemistry—A European Journal

Full Paper
doi.org/10.1002/chem.202100462

Chemistry
Europe
European Chemical
Societies Publishing

straightforward because of large shifts relative to DnaB:Mg^{2+}. The assignments obtained by comparing the DnaB:Mg^{2+} spectra (for which the sequential resonance assignment had been performed[5]) with the DnaB:Co^{2+} spectra were validated by pairwise comparison of the PCSs of ^{15}N, ^{13}C$^{\alpha}$ and ^{13}C$^{\beta}$ (Figure 2c). The PCS values for nuclei of the same residue should be similar due to comparable distances between these atoms and the paramagnetic center. The linear correlation in these pairwise comparisons thus indicates a plausible assignment for the DnaB:Co^{2+} sample.

Structure calculation

The determination of the metal ion position based on the paramagnetic restraints was performed in CYANA.[40,41] The structure calculation protocol comprises four steps (Figure S4): dataset preparation, regularization, determination of the metal ion position, and PCS tensor determination. The input data for the CYANA calculations were obtained from the spectra of DnaB:Mn^{2+} and DnaB:Co^{2+} and are summarized in Table 1.

The starting model of *Hp*DnaB was based on the *Aa*DnaB:ADP:Mg^{2+} complex for which a crystal structure at 3.3 Å resolution has been reported.[42] The *Hp*DnaB-CTD monomers (PDB accession codes 3GXV and 4A1F) were superimposed on the *Aa*DnaB-CTD structure (PDB accession code 4NMN) maintaining the oligomeric arrangement of the initial crystal structure. The resulting van-der-Waals restraint violations, mostly at the interface between the DnaB monomers, were reduced in the initial simulating annealing step (called regularization in CYANA, for more details see Methods section in the Supporting Information). Note that the metal ion cofactor in the *Aa*DnaB:ADP complex is not localized with high precision as it does not lead to a well-defined electron density and shows a large temperature coefficient in the order of 60 Å^2. As starting point for the next phase (optimization of the metal ion position) the regularized structure (with backbone RMSD backbone 0.11 Å to the initial model) is used.

The metal ion position was determined using CYANA by employing the two classes of long-range distance restraints introduced above. The first class (residues broadened beyond detection) was used to determine the upper distance limit (upl) which defines the radius of the blind sphere of Mn^{2+} in which all residues are broadened beyond detection. The second one ($I_{para}/I_{dia} \geq 0.6$) was used to determine the lower distance limit

(lol) above which the residues should not be affected by any PRE effect. One metal ion affects two DnaB monomers, since the NBDs are located in-between two DnaB monomers in the oligomeric DnaB assembly[43] (see also Figure S6).

First, only restraints of class (i) were considered. The optimal upl-value was found for the 3D NCACB experiment by systematically changing the upl-value in steps of 1.0 Å and evaluating the CYANA target function (pseudoenergy).[44] The resulting "L-curve" (Figure S7, left panels) shows, as expected, that the target function decreases with increasing the upl-value. No clustering of the metal ion position in the obtained structural bundle was observed for upl values below 8 Å or above 18 Å (Figure S7c). Based on Figure S7b, an upper bound of 15 Å was chosen for the blind sphere of Mn^{2+}, resulting in 177 distance restraints per monomer of which 24 per monomer are violated (Table S4; two strongly violated restraints were discarded).

In a second step, the lol-values were included in the calculations using the restraints of class (ii). Again, the lol-value was determined by a (mirrored) "L-curve" as described above (Figure S7, right panels). A lower bound of 18 Å was chosen for the subsequent calculations, resulting in 9 violated distance restraints per monomer (Table S5; all violations are smaller than 1 Å).

The blind sphere for Co^{2+} was determined by keeping the metal position found for the Mn^{2+} case fix and by screening the number of violations over a distance range in steps of 0.5 Å (0.01 to 30 Å). The upl-value was determined in this case to 14 Å (Figure S5). It turns out that the blind spheres of Mn^{2+} and Co^{2+} have similar radii, but that, as stated above, in case of Co^{2+} this is mostly not caused by PRE but by the anisotropic component of the spin-dipolar coupling broadening the NMR resonances substantially.[35–36]

In total, around 200 PCSs from N, C$^{\alpha}$ and C$^{\beta}$ chemical shifts extracted from 2D NCA and 3D NCACB spectra were used to determine the PCS tensor orientation. Theoretically, only eight unambiguous and precise PCSs would be required to determine the three Cartesian coordinates of the Co^{2+} metal ion position, the three Euler angles, as well as $\Delta\chi_{ax}$ and $\Delta\chi_{rh}$. However, the hexameric nature of DnaB has the consequence that the PCSs are not all caused by the metal center in the same DnaB monomer. Therefore the calculations were always done using the entire hexamer. For that purpose, the two $\Delta\chi$-tensor components, $\Delta\chi_{ax}$ and $\Delta\chi_{rh}$, were systematically varied in CYANA and in total 870 calculations were performed (Figure S8). The result of this screening shows a minimal number of

Table 1. Summary of all paramagnetic data extracted from the 3D NCACB spectra. The number of restraints contains the number of restraints per monomer for the backbone N, Cα and Cβ atoms.

Sample	Type of effect	No. of restraints[a]	Used in phase of protocol[b]	Restraint class in CYANA[b]
DnaB:Mn^{2+}	Peak invisible	177	metal ion position	Upper distance limit (15 Å)
	PRE > 0.6	57	optimization of metal ion position	Lower distance limit (18 Å)
	PRE < 0.6	135	PCS tensor determination	Distance limit > 15 Å and < 18 Å
DnaB:Co^{2+}	Peak invisible	123	–[c]	Upper distance limit (14 Å)
	PCS	199	PCS tensor determination	pcs

[a] Contains for each amino acid three restraints: N, C$^{\alpha}$ and C$^{\beta}$, except for glycines for which only N and Cα are considered. [b] See Figure S4 for details. [c] These restraints are used for back-calculation of the blind sphere of Co^{2+} (Figure S5 and violated restraints in Table S3).

Chemistry–A European Journal

Full Paper
doi.org/10.1002/chem.202100462

Chemistry Europe
European Chemical
Societies Publishing

violated PCSs restraints for $\Delta\chi_{ax} = 5.2 \times 10^{-32}$ m^3 and $\Delta\chi_{rh} = 2.9 \times 10^{-32}$ m^3 (Figure S8), comparable to other published values.[45–47] The linear correlation between experimental and calculated PCSs using these $\Delta\chi$ tensor parameter is given in Figure 3a. PCSs are considered as violated if the deviation between calculated and experimental value is larger than 0.5 ppm. The value of 0.5 ppm was chosen based on the limited digital resolution, particularly in the ^{15}N dimensions of the NMR spectra, caused by the required high power ^{1}H radiofrequency

decoupling during the detection and evolution periods of the experiment. Using this threshold, 1140 of the 1194 back-calculated PCSs agree with the experimental values. Figure 3b shows the PCS iso-surface plotted on the structural model.

The results of the structure calculation are summarized in Table 2. Overall, around 89% of the upl, lol and PCS restraints are fulfilled, which is reasonable in light of the experimental limitations (e.g. spectral resolution, incomplete assignment) and the starting model obtained by homology modelling. A few distance restraints are strongly violated and would have a strong effect on the final metal ion position. These include D261 and C271 (from DnaB:Mn^{2+}) and R259, C271 and I331 (from DnaB:Co^{2+}).

Determination of Mn^{2+} electronic relaxation times

The magnitude of the PRE-effect in solids is governed by the electronic relaxation time (see Eqs. (3) and (4)) and affects the NMR signal attenuations detected. The expected signal attenuation in the performed NMR experiment can be calculated as a function of the distance between the paramagnetic center and the residue of interest.[31] The signal-attenuation curves for Mn^{2+} for 2D DARR and 3D NCACB spectra are shown in Figure 4 together with theoretical curves assuming T_{1e} relaxation times of 5, 15 and 40 ns. And indeed, the experimental data points follow the predicted curves allowing to determine the Mn^{2+} T_{1e}-value to around 15 ns comparable with published value.[49]

Discussion of the result of the structure calculation and DNA localization

Figure 5a shows the initial position and 5b the result of the structure calculation for the the metal ions (blue spheres). The metal ions of the ten lowest energy structures (25 structures were calculated in total; the target function values of the 10 selected structures are within 5% of that of the best structure) cluster at specific positions by only using paramagnetic distance restraints from solid-state NMR. A closer view into the NBD (Figure 5c) shows that the metal ion positions obtained from different structure calculation cycles indeed cluster (RMSD backbone atoms for the 10 lowest energy structures: 0.16 ± 0.01 Å and RMSD metal ions for the ten lowest energy structures: 0.06 ± 0.03 Å). The number of calculated structures
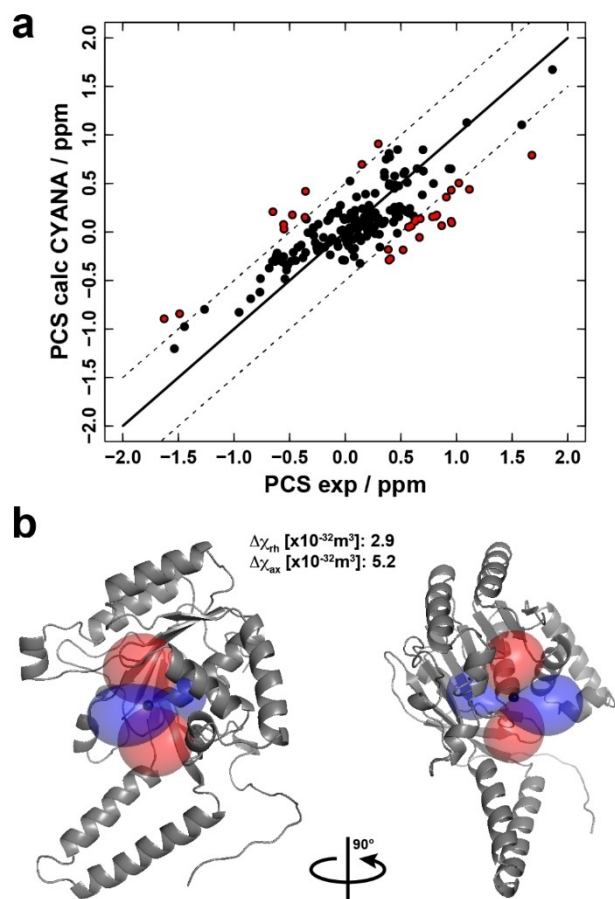

Figure 3. Determination of the $\Delta\chi$-tensor orientation. **a.** Correlation between experimental and calculated PCSs. The black line indicates a perfect linear correlation between experimental and calculated PCSs. The dashed lines show deviations of ± 0.5 ppm. Black and red points show the accepted and violated PCS, respectively. **b.** PCS iso-surface plotted on a monomer of *Hp*DnaB using PyMOL.[48] Blue and red surfaces indicate PCS values of $+1.0$ ppm and -1.0 ppm, respectively.

Table 2. Summary of the used paramagnetic restraints.

Sample	Restraint class in CYANA	Used in phase of protocol	No. of restraints	No. of violated restraints[a]
DnaB:Mn^{2+}	upl	optimization of metal ion position	171 (+6)[b]	18 (+6)[b]
	lol	optimization of metal ion position	57	9
	upl	PCS tensor determination	135	0[c]
	lol		135	29[c]
DnaB:Co^{2+}	upl	–	111 (+12)[b]	11 (+12)[b]
	PCS	PCS tensor determination	199	9[d]

[a] PRE restraint violated by more than 0.001 Å. [b] Excluded from the final structure calculation (D261 and C271 for DnaB:Mn^{2+}; S219, R259, C271 and I331 for DnaB:Co^{2+}). [c] See violated restraints in Table S7 and S8. [d] PCS restraints violated by more than 0.5 ppm.
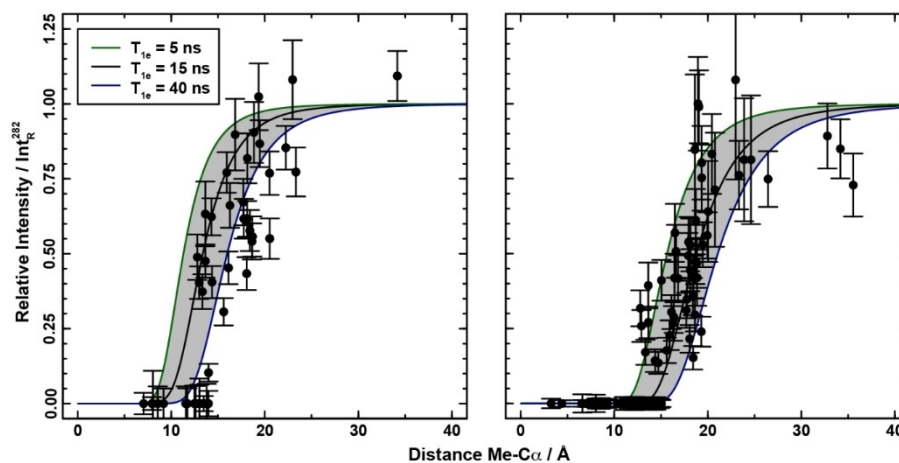
Chemistry–A European Journal

Full Paper
doi.org/10.1002/chem.202100462

Chemistry Europe
European Chemical
Societies Publishing

Figure 4. Determination of Mn^{2+} electronic relaxation time. Signal decay profile of a 2D ^{13}C–^{13}C DARR 20 ms (left) and a 3D NCACB (right) by PRE of Mn^{2+} ($S = 5/2$) for three different T_{1e} values. The calculations were performed as described in reference [31] using the expressions in the Supporting Information and parameters in Table S6.
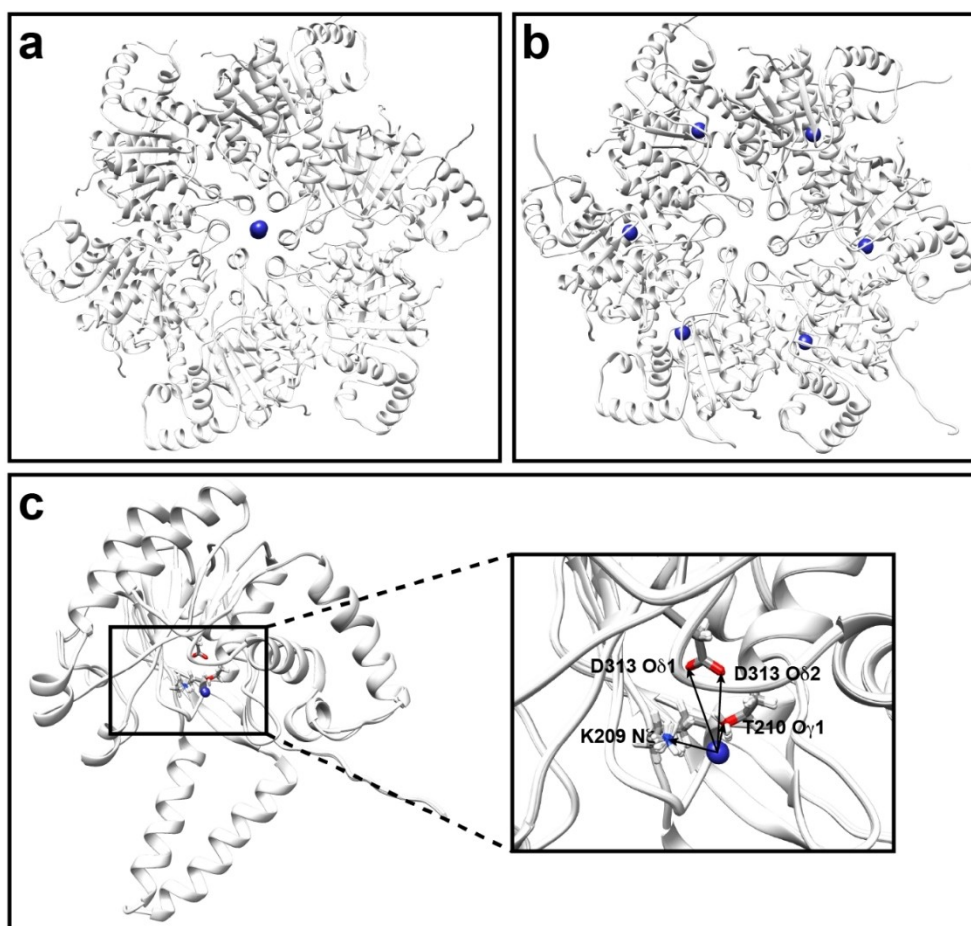

Figure 5. Result of the metal ion localization calculation. **a.** Model of DnaB-CTD before optimization of the metal ion position (the 10 lowest energy structures are given, see Figure S9). **b.** Model showing the optimized metal ion position. The number of restraints violated more than 0.2 Å is 80 ± 3 (upl) and 44 ± 1 (lol). **c.** Monomer of HpDnaB-CTD (the 10 lowest energy structures are shown) and zoom into the NBD (residues K209, T210 and D313 are highlighted). The arrows indicate the binding of the metal ion to possible binding sites.

Chemistry–A European Journal

Full Paper
doi.org/10.1002/chem.202100462

Chemistry Europe
European Chemical
Societies Publishing

does not influence the precision of the calculation significantly, as indicated by rather similar RMSD values of 0.05 ± 0.01 Å, 0.06 ± 0.02 Å and 0.07 ± 0.02 Å, respectively, for the metal ion positions considering the 10, 20 and 40 structures with lowest target function values from a structure calculation run with 100 structures. The observed clustering is a consequence of a sufficiently large set of distance restraints and a starting model that describes the structure of DnaB reasonably well. Figure S9 shows for comparison the metal ion position found in the X-Ray structure of the DnaB helicase from *Geobacillus stearothermophilus* (*Bst*Dnab; PDB 4ESV, chain D)[50] which belongs to the same superfamily of helicases as *Hp*DnaB. In both cases, the metal ion is located close to characteristic residues involved in binding the metal ion cofactor, such as a threonine (T210) of the Walker A motif as well as the aspartate of the Walker B motif (D313). The distances between the metal center and the aspartate of the Walker B motif were determined to 6.0 vs 3.7 Å (M^{2+}-OD1) and 6.1 vs. 6.7 Å (M^{2+}-OD2) for *Hp*DnaB compared to *Bst*DnaB, whereas the distances to the threonine of the Walker A motif are quite similar (2.4 vs. 2.1 Å, M^{2+}-OG1). Paramagnetic restraints alone are thus suitable to locate the metal ion de-novo in the right position, even by using an arbitrary starting position, e.g. in the middle of the hexamer, as shown in Figure 5a.

It remains an open question how the DNA binds exactly within the inner pore of the helicase. The present paramagnetic solid-state NMR approach reveals, through the measurements of the ^{31}P PCSs of the two DNA phosphate groups binding to DnaB5, their location relative to the Co^{2+} metal ion. Figure 6a shows the ^{1}H-^{31}P CPMAS spectra of DnaB:Mg^{2+} and DnaB:Co^{2+}. The spectra of both complexes show two resonances, P1 and P2, for the bound DNA (dT$_{20}$) reflecting the DNA:DnaB monomer ratio of 2:1.[5] The ^{31}P PCSs are determined to 0.7 ppm for P1 and 0.6 ppm for P2. Figure 6b shows the corresponding two PCS-surfaces based on the metal ion position and $\Delta\chi$-tensor components discussed before, colored in dark (P2) and light blue (P1). The DNA phosphate groups must be located on this surface and indeed, residues located in the DNA-binding loop identified in coordinating DNA,[51] e.g. K373, D374 and G376, are oriented towards these PCS surface (Figure 6b) even without a further structural re-optimization of the DNA binding loops.

Conclusions

We here derived, using paramagnetic substitutions of the ATP Mg^{2+} cofactor, the localization of the metal ion in the oligomeric DnaB:ADP:AlF$_4^-$:DNA complex, as well as the location of the DNA phosphate groups in the inner pore of the helicase. This was enabled through paramagnetic solid-state NMR, in combination with sequential resonance assignments and a structural homology model. The structure calculation protocol implemented in CYANA is based on PRE restraints extracted from multidimensional solid-state NMR spectra. PCSs induced by Co^{2+} determine the $\Delta\chi$-tensor components of Co^{2+}.
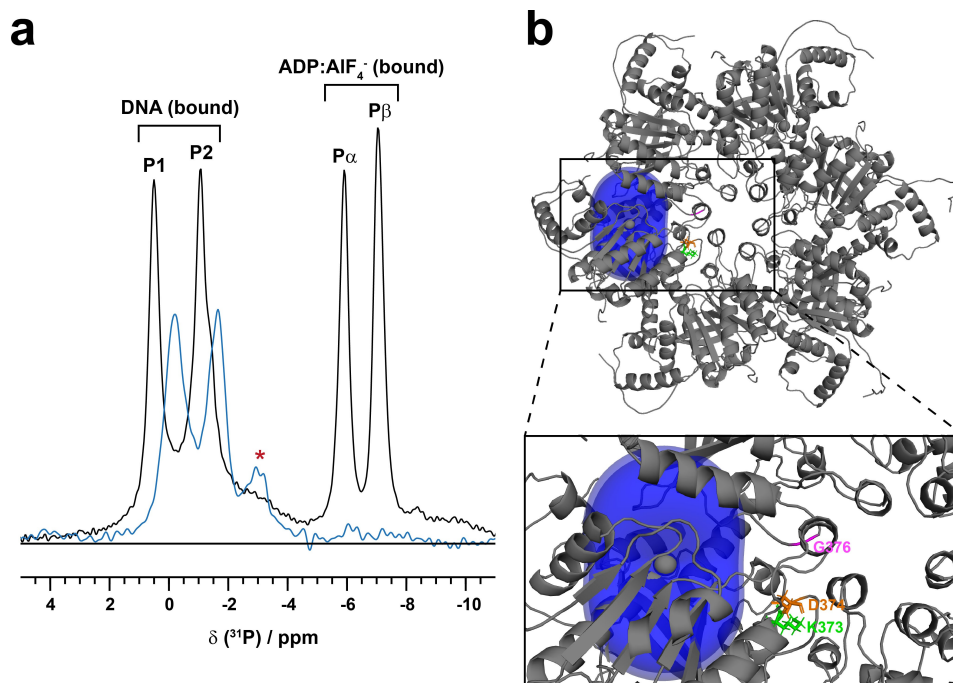

Figure 6. *Phosphorus MAS NMR to position the DNA phosphate groups.* **a.** ^{1}H-^{31}P CPMAS of DnaB:Mg^{2+} (black), and DnaB:Co^{2+} (blue). The assignment of the diamagnetic sample is taken from reference [5]. The two spectra are scaled to the same noise level. The red star marks a possible impurity. The spectrum of DnaB:Mg^{2+} was taken from reference[5] (http://creativecommons.org/licenses/by/4.0). **b.** ^{31}P PCS isosurfaces of 0.6 ppm (the PCS of P2) and 0.7 ppm (the PCS of P1) plotted on the DnaB structure obtained after metal ion position optimization. The DNA phosphate groups that give rise to the resonances P1 and P2 must be located on these surfaces. Characteristic residues located in the DNA-binding loop are highlighted.

The PCSs of the ^{31}P resonances of DNA is used to restrain the location of the DNA phosphate groups. The proposed approach allowed to obtain first structural information on binding partners in this large ATP-fueled protein engine and illustrates the potential of paramagnetic solid-state NMR on large ATP-fueled motor proteins.

Experimental Section

*Hp*DnaB samples for solid-state NMR

^{13}C—^{15}N labelled *Hp*DnaB was prepared in buffer A (2.5 mM sodium phosphate, pH 7.5, 130 mM NaCl) as described in reference.[21] All protein solutions were sedimented[20–21,23,46] in the MAS-NMR rotor (16 h at 4 °C at 210,000×g) using home-built tools.[52]

*Hp*DnaB:ADP:AlF$_4^-$:MgCl$_2$:DNA complex (DnaB:Mg^{2+})

0.3 mM *Hp*DnaB in buffer A was mixed with 5 mM MgCl$_2$·H$_2$O and consecutively 6 mM NH$_4$AlF$_4$ solution (prepared by incubating 1 M AlCl$_3$ solution with 5-fold excess of 1 M NH$_4$F solution (compared to AlF$_3$) for 5 min in H$_2$O) and 5 mM ADP and incubated for 2 h at 4 °C. 1 mM of (dT)$_{20}$ (DNA, purchased from Microsynth) was added to the complex and reacted for 30 min at r.t.

*Hp*DnaB:ADP:AlF$_4^-$:MnCl$_2$:DNA complex (DnaB:Mn^{2+})

0.3 mM *Hp*DnaB in buffer A was mixed with 1.4 mM MnCl$_2$·H$_2$O (5-fold molar excess compared to an *Hp*DnaB monomer) and consecutively 6 mM NH$_4$AlF$_4$ solution (prepared by incubating 1 M AlCl$_3$ solution with 5-fold excess of 1 M NH$_4$F solution (compared to AlF$_3$) for 5 min in H$_2$O) and 5 mM ADP and incubated for 2 h at 4 °C. 1 mM of (dT)$_{20}$ was added to the complex and reacted for 30 min at r.t. Note that an approx. 5-fold excess of Mn^{2+} (compared to a DnaB monomer) was used to avoid a too high excess of unbound Mn^{2+} that could bind unspecifically to the protein.[32]

*Hp*DnaB:ADP:AlF$_4^-$:CoCl$_2$:DNA complex (DnaB:Co^{2+})

0.3 mM *Hp*DnaB in buffer A was mixed with 5.4 mM CoCl$_2$·H$_2$O (18-fold molar excess compared to an *Hp*DnaB monomer) and consecutively 6 mM NH$_4$AlF$_4$ solution (prepared by incubating 1 M AlCl$_3$ solution with 5-fold excess of 1 M NH$_4$F solution (compared to AlF$_3$) for 5 min in H$_2$O) and 5 mM ADP and incubated for 2 h at 4 °C. 1 mM of (dT)$_{20}$ was added to the complex and reacted for 30 min at r.t. Note that an approx. 18-fold excess of Co^{2+} (compared to a DnaB monomer) was used to saturate all binding sites.

Solid-state NMR experiments

^{13}C-detected solid-state NMR spectra were acquired at 20.0 T static magnetic field strength using a 3.2 mm Bruker Biospin E-free probe and ^{31}P-detected spectra were recorded at 11.7 T using a Bruker 3.2 mm Bruker Biospin probe. The MAS frequency was set to 17.0 kHz in both cases. The sample temperature was set to 278 K using the water line as an internal reference.[52] The spectra were processed with the software TOPSPIN (version 3.5, Bruker Biospin) with a shifted (2.5 to 3.0) squared cosine apodization function and automated baseline correction in the indirect and direct dimension. An overview of the experimental parameters for all NMR spectra is given in Table S9. Spectra were analyzed with the software CcpNmr[53–55] (version 2.4.2) and referenced to 4,4-dimethyl-4-

silapentane-1-sulfonic acid (DSS). The assignment of the complex DnaB:Mg^{2+} is taken from reference.[5]

CYANA calculations

All structure calculations were performed with CYANA (version 3.98.10).[40,41] The CYANA calculations are split into three independent steps. The first step (regularization) is needed to adapt the *Hp*DnaB model to the CYANA standard geometry, to insert the metal ion, and to improve the model with respect to symmetry and van-der-Waals restraint violations. In the second step, the metal ion position is optimized with long-range distance restraints (upl and lol) extracted from 3D NCACB spectra of DnaB:Mg^{2+} and DnaB:Mn^{2+}. All distance restraints are treated as ambiguous distance restraints to two metal ions. In a third step, CYANA was extended by a new macro for the determination of the PCS tensor. All CYANA codes for all three steps are given in the Supporting Information.

Structural model of *Hp*DnaB

The hexameric crystal structure of *Aa*DnaB:ADP (resolution 3.3 Å, PDB accession code 4NMN) was used as a template to build an hexameric model of the *Hp*DnaB-CTD:ADP complex. Six individual monomers of *Hp*DnaB-CTD (PDB accession code 4 A1F) were superimposed to six subunits of the *Aa*DnaB hexamer (rmsd of 1.365 Å for 213 Cα). The ADP and Mg^{2+} coordinates present at the interfaces of the *Aa*DnaB:ADP model were merged to the six *Hp*DnaB CTDs to generate the hexamer of *Hp*DnaB:ADP. Note, that the ADP and Mg^{2+} atoms were not used in the structure calculations described herein. Flexible linkers between the monomers were inserted into the model for the CYANA calculation. These linkers contain in total 11 dummy atoms (no van-der-Waals radius) with a distance between them of 2 Å.

This initial model exhibited 1039 van-der-Waals restraint violations larger than 0.2 Å. Most of these violations are caused by steric clashes between side-chain atoms in neighboring monomers. These are reduced in CYANA by employing the so-called "regularization" algorithm which calculates a regularized structure in torsion angle space which is as close as possible to the initial structure, but exhibits ideal covalent geometries and reduced van-der-Waals violations.[56–58] Six metal ions were added before regularization. The ion radius was set to 0.66 Å in all calculations. C$_6$-symmetry was introduced by symmetry-related distance difference restraints (weighting factor 0.025)[59] between all six monomers and also between all six metal ions. This symmetry assumption is based on the absence of peak doubling in the NMR spectra and the presence of a hexamer in the crystal structure of *Aa*DnaB:ADP. Regularization reduced the CYANA target function from 1886 to 73 Å^2 and the number of van-der-Waals restraint violations from 1029 to 250. Structural changes during regularization are overall negligible (backbone RMSD 0.11 Å; Figure S10a). The largest differences between the two structures before and after regularization (changes in atomic coordinates > 1.0 Å) are located in the center of the hexameric structure of *Hp*DnaB (Figure S10b: α-helix in the center of the model) for which no electron density was observed in the crystal structure of the CTD of *Hp*DnaB used herein.[4] Gly and Pro restraints are not included in the calculation, the first due to their absence and the second due to their weak signals in NCACB spectra.

Long-range restraints

Long-range restraints are classified as upper-distance limits (upl; 177 restraints per monomer, 1062 restraints for the hexameric model) and lower-distance limits (lol; 57 per monomer, 342 for the hexamer). Two non-visible peaks were not included into the calculation (D261 and C271). D261 and C271 are strongly violated in the calculations (by 12.5 and 7.9 Å). D261 and C271 are located in the same α-helix (Figures S11 and S12). Possibly, the cysteine is oxidized by oxidized manganese ions (such as Mn^{4+}), which leads to the disappearance of the reduced cysteine from the spectra. Alternatively, assignment errors or a stronger structural deviation from the starting structure might explain the violations observed for these residues.

PRE determination

PREs were determined using the quotient of the intensities (peak heights) extracted from the diamagnetic and paramagnetic samples. For normalization, the peak of amino acid F282, which is isolated in the 3D spectra and in the structural model far part from the NBD was used. The error bars of the PREs in Figure 2a were determined by error propagation based on the contribution of the noise in both 3D NCACB spectra (Mg^{2+} and Mn^{2+}).

PCS determination

The assignment of the DnaB:Co^{2+} spectra was done by comparing the DnaB:Mg^{2+} spectra with the ones of DnaB:Co^{2+}. ^{15}N, $^{13}C^{\alpha}$, $^{13}C^{\beta}$ PCSs (in total 199 PCSs per monomer) were extracted from the 2D 15 N–^{13}C NCA, 2D ^{13}C–^{13}C 20 ms DARR and 3D NCACB spectra. The ^{15}N PCSs were only collected from the 2D ^{15}N–^{13}C NCA, since the 3D spectra suffer from a too low digital resolution in the indirect ^{15}N dimension.

PCS calculations

PCSs were used as orientation restraints in CYANA. A grid search over a broad range of $\Delta\chi_{ax}$ and $\Delta\chi_{rh}$ values (in steps of 0.93×10^{-32} m^3 for $\Delta\chi_{ax}$ and 0.27×10^{-32} m^3 for $\Delta\chi_{rh}$) with in total 870 simulations was performed to find the orientation of the PCS tensor leading to the lowest CYANA target function value.

Author contributions

RC prepared the samples. JZ and TW performed the NMR experiments. JZ and PG carried out the CYANA calculations. LT provided the DnaB structural model. JZ, TW, LT, ME, PG, AB, and BHM analyzed the data. All authors contributed to the writing of the manuscript. PG, BHM, and TW designed and supervised the research.

Acknowledgements

Conflict of Interest

The authors declare no conflict of interest.

[1] M. P. Williamson, *Prog. Nucl. Magn. Reson. Spectrosc.* **2013**, *73*, 1–16.
[2] M. Tong, J. G. Pelton, M. L. Gill, W. Zhang, F. Picart, M. A. Seeliger, *Nat. Commun.* **2017**, *8*, 2160.
[3] C. P. Jaroniec, *J. Magn. Reson.* **2015**, *253*, 50–59.
[4] M. Stelter, I. Gutsche, U. Kapp, A. Bazin, G. Bajic, G. Goret, M. Jamin, J. Timmins, L. Terradot, *Structure* **2012**, *20*, 554–564.
[5] T. Wiegand, R. Cadalbert, D. Lacabanne, J. Timmins, L. Terradot, A. Böckmann, B. H. Meier, *Nat. Commun.* **2019**, *10*, 31.
[6] J. Snider, G. Thibault, W. A. Houry, *Genome Biol.* **2008**, *9*, 216.
[7] V. Gaponenko, S. P. Sarma, A. S. Altieri, D. A. Horita, J. Li, R. A. Byrd, *J. Biomol. NMR* **2004**, *28*, 205.
[8] G. Pintacuda, N. Giraud, R. Pierattelli, A. Böckmann, I. Bertini, L. Emsley, *Angew. Chem. Int. Ed.* **2007**, *46*, 1079–1082; *Angew. Chem.* **2007**, *119*, 1097–1100.
[9] S. Balayssac, I. Bertini, A. Bhaumik, M. Lelli, C. Luchinat, *Proc. Natl. Acad. Sci. USA* **2008**, *105*, 17284–17289.
[10] H. W. Orton, G. Otting, *J. Am. Chem. Soc.* **2018**, *140*, 7688–7697.
[11] A. Bahramzadeh, T. Huber, G. Otting, *Biochemistry* **2019**, *58*, 3243–3250.
[12] A. Dalaloyan, A. Martorana, Y. Barak, D. Gataulin, E. Reuveny, A. Howe, M. Elbaum, S. Albeck, T. Unger, V. Frydman, E. H. Abdelkader, G. Otting, D. Goldfarb, *ChemPhysChem* **2019**, *20*, 1860–1868.
[13] M. Ahmed, A. Marchanka, T. Carlomagno, *Angew. Chem. Int. Ed.* **2020**, *59*, 6866–6873; *Angew. Chem.* **2020**, *132*, 6933–6940.
[14] M. Ubbink, M. Ejdebäck, B. G. Karlsson, D. S. Bendall, *Structure* **1998**, *6*, 323–335.
[15] C. Schmitz, R. Vernon, G. Otting, D. Baker, T. Huber, *J. Mol. Biol.* **2012**, *416*, 668–677.
[16] J. Li, K. B. Pilla, Q. Li, Z. Zhang, X. Su, T. Huber, J. Yang, *J. Am. Chem. Soc.* **2013**, *135*, 8294–8303.
[17] M. P. Foster, C. A. McElroy, C. D. Amero, *Biochemistry* **2007**, *46*, 331–340.
[18] D. P. Frueh, A. C. Goodrich, S. H. Mishra, S. R. Nichols, *Curr. Opin. Struct. Biol.* **2013**, *23*, 734–739.
[19] T. Wiegand, *Prog. Nucl. Reson. Spectrosc.* **2020**, *117*, 1–32.
[20] I. Bertini, C. Luchinat, G. Parigi, E. Ravera, B. Reif, P. Turano, *Proc. Natl. Acad. Sci. USA* **2011**, *108*, 10396–10399.
[21] C. Gardiennet, A. K. Schütz, A. Hunkeler, B. Kunert, L. Terradot, A. Böckmann, B. H. Meier, *Angew. Chem. Int. Ed.* **2012**, *51*, 7855–7858; *Angew. Chem.* **2012**, *124*, 7977–7980.
[22] D. Lacabanne, M. L. Fogeron, T. Wiegand, R. Cadalbert, B. H. Meier, A. Böckmann, *Prog. Nucl. Magn. Reson. Spectrosc.* **2019**, *110*, 20–33.
[23] T. Wiegand, D. Lacabanne, A. Torosyan, J. Boudet, R. Cadalbert, F. H. Allain, B. H. Meier, A. Böckmann, *Front. Mol. Biosci.* **2020**, *7*, 17.
[24] G. Otting, *J. Biomol. NMR* **2008**, *42*, 1–9.
[25] S. Balayssac, I. Bertini, M. Lelli, C. Luchinat, M. Maletta, *J. Am. Chem. Soc.* **2007**, *129*, 2218–2219.
[26] C. P. Jaroniec, *Solid State Nucl. Magn. Reson.* **2012**, *43–44*, 1–13.
[27] G. Otting, *Annu. Rev. Biophys.* **2010**, *39*, 387–405.
[28] J. Koehler, J. Meiler, *Prog. Nucl. Magn. Reson. Spectrosc.* **2011**, *59*, 360–389.
[29] I. Solomon, *Phys. Rev.* **1955**, *99*, 559–565.
[30] N. Bloembergen, L. O. Morgan, *J. Chem. Phys.* **1961**, *34*, 842–850.
[31] H. Tamaki, A. Egawa, K. Kido, T. Kameda, M. Kamiya, T. Kikukawa, T. Aizawa, T. Fujiwara, M. Demura, *J. Biomol. NMR* **2016**, *64*, 87–101.
[32] T. Wiegand, D. Lacabanne, K. Keller, R. Cadalbert, L. Lecoq, M. Yulikov, L. Terradot, G. Jeschke, B. H. Meier, A. Böckmann, *Angew. Chem. Int. Ed.* **2017**, *56*, 3369–3373; *Angew. Chem.* **2017**, *129*, 3418–3422.
[33] M. J. Knight, I. C. Felli, R. Pierattelli, L. Emsley, G. Pintacuda, *Acc. Chem. Res.* **2013**, *46*, 2108–2116.
[34] I. Bertini, C. Luchinat, S. Aime, *Coord. Chem. Rev.* **1996**, *150*, 77–110.

[35] I. Bertini, L. Emsley, M. Lelli, C. Luchinat, J. Mao, G. Pintacuda, *J. Am. Chem. Soc.* **2010**, *132*, 5558–5559.

[36] A. J. Pell, G. Pintacuda, C. P. Grey, *Prog. Nucl. Magn. Reson. Spectrosc.* **2019**, *111*, 1–271.

[37] R. K. Soni, P. Mehra, N. R. Choudhury, G. Mukhopadhyay, S. K. Dhar, *Nucleic Acids Res.* **2003**, *31*, 6828–6840.

[38] K. Takegoshi, S. Nakamura, T. Terao, *J. Chem. Phys.* **2003**, *118*, 2325–2341.

[39] M. Baldus, A. T. Petkova, J. Herzfeld, R. G. Griffin, *Mol. Phys.* **1998**, *95*, 1197–1207.

[40] P. Güntert, C. Mumenthaler, K. Wüthrich, *J. Mol. Biol.* **1997**, *273*, 283–298.

[41] P. Güntert, L. Buchner, *J. Biomol. NMR* **2015**, *62*, 453–471.

[42] M. S. Strycharska, E. Arias-Palomo, A. Y. Lyubimov, J. P. Erzberger, V. L. O'Shea, C. J. Bustamante, J. M. Berger, *Mol. Cell* **2013**, *52*, 844–854.

[43] M. Spies, *DNA helicases and DNA motor proteins*, Springer, New York, **2013**.

[44] P. Güntert, *Methods Mol. Biol.* **2004**, *278*, 353–378.

[45] R. Georgescu, Z. Yuan, L. Bai, R. de Luna Almeida Santos, J. Sun, D. Zhang, O. Yurieva, H. Li, M. E. O'Donnell, *Proc. Natl. Acad. Sci. USA* **2017**, *114*, E697-E706.

[46] C. Gardiennet, T. Wiegand, A. Bazin, R. Cadalbert, B. Kunert, D. Lacabanne, I. Gutsche, L. Terradot, B. H. Meier, A. Böckmann, *J. Biomol. NMR* **2016**, *64*, 189–195.

[47] L. Benda, J. Mares, E. Ravera, G. Parigi, C. Luchinat, M. Kaupp, J. Vaara, *Angew. Chem. Int. Ed.* **2016**, *55*, 14713–14717; *Angew. Chem.* **2016**, *128*, 14933–14937.

[48] V. S. The PyMOL Molecular Graphics System, LLC.

[49] J. Malanho Silva, L. Cerofolini, S. Giuntini, V. Calderone, C. Geraldes, A. L. Macedo, G. Parigi, M. Fragai, E. Ravera, C. Luchinat, *J. Struct. Biol.* **2019**, *206*, 99–109.

[50] O. Itsathitphaisarn, R. A. Wing, W. K. Eliason, J. Wang, T. A. Steitz, *Cell* **2012**, *151*, 267–277.

[51] T. Wiegand, M. Schledorn, A. A. Malär, R. Cadalbert, A. Däpp, L. Terradot, B. H. Meier, A. Böckmann, *ChemBioChem* **2020**, *21*, 324–330.

[52] A. Böckmann, C. Gardiennet, R. Verel, A. Hunkeler, A. Loquet, G. Pintacuda, L. Emsley, B. H. Meier, A. Lesage, *J. Biomol. NMR* **2009**, *45*, 319–327.

[53] R. Fogh, J. Ionides, E. Ulrich, W. Boucher, W. Vranken, J. P. Linge, M. Habeck, W. Rieping, T. N. Bhat, J. Westbrook, K. Henrick, G. Gilliland, H. Berman, J. Thornton, M. Nilges, J. Markley, E. Laue, *Nat. Struct. Biol.* **2002**, *9*, 416–418.

[54] W. F. Vranken, W. Boucher, T. J. Stevens, R. H. Fogh, A. Pajon, M. Llinas, E. L. Ulrich, J. L. Markley, J. Ionides, E. D. Laue, *Proteins* **2005**, *59*, 687–696.

[55] T. J. Stevens, R. H. Fogh, W. Boucher, V. A. Higman, F. Eisenmenger, B. Bardiaux, B. J. van Rossum, H. Oschkinat, E. D. Laue, *J. Biomol. NMR* **2011**, *51*, 437–447.

[56] P. Güntert, *Methods Mol. Biol.* **1997**, *60*, 157–194.

[57] D. Gottstein, S. Reckel, V. Dötsch, P. Güntert, *Structure* **2012**, *20*, 1019–1027.

[58] D. Gottstein, D. K. Kirchner, P. Güntert, *J. Biomol. NMR* **2012**, *52*, 351–364.

[59] Y. J. Lin, D. K. Kirchner, P. Güntert, *J. Magn. Reson.* **2012**, *222*, 96–104.